PROCEEDINGS OF SPIE

SPIEDigitalLibrary.org/conference-proceedings-of-spie

# Performance of the advanced ACTPol low frequency array

Li, Yaqiong, Austermann, Jason , Beall, James, Bruno, Sarah Marie, Choi, Steve, et al.

Yaqiong Li, Jason E. Austermann, James A. Beall, Sarah Marie Bruno, Steve K. Choi, Nicholas F. Cothard, Kevin T. Crowley, Shannon M. Duff, Patricio A. Gallardo, Shawn W. Henderson, Shuay-Pwu Patty Ho, Johannes Hubmayr, Brian J. Koopman, Jeff J. McMahon, Michael D. Niemack, Maria Salatino, Sara M. Simon, Suzanne T. Staggs, Jason R. Stevens, Joel N. Ullom, Jonathan Ward, Edward J. Wollack, "Performance of the advanced ACTPol low frequency array ," Proc. SPIE 10708, Millimeter, Submillimeter, and Far-Infrared Detectors and Instrumentation for Astronomy IX, 107080A (24 July 2018); doi: 10.1117/12.2313942

SPIE.

Event: SPIE Astronomical Telescopes + Instrumentation, 2018, Austin, Texas, United States

# Performance of the Advanced ACTPol Low Frequency Array

Yaqiong Li*[a]; Jason E. Austermann[b]; James A. Beall[b]; Sarah Marie Bruno[a]; Steve K. Choi[a]; Nicholas F. Cothard[c]; Kevin T. Crowley[a]; Shannon M. Duff[b]; Patricio A. Gallardo[c]; Shawn W. Henderson[c]; Shuay-Pwu Patty Ho[a]; Johannes Hubmayr[b]; Brian J. Koopman[c]; Jeff J. McMahon[d]; Michael D. Niemack[c]; Maria Salatino[a]; Sara M. Simon[d]; Suzanne T. Staggs[a]; Jason R. Stevens[c]; Joel N. Ullom[b]; Jonathan Ward[e]; Edward J. Wollack[f];

[a]Department of Physics, Princeton University, Princeton, NJ, USA 08540
[b]NIST Quantum Devices Group, 325 Broadway Mailcode 817.03, Boulder, CO, USA 80305
[c]Department of Physics, Cornell University, Ithaca, NY, USA 14853
[d]Department of Physics, Michigan University, Ann Arbor, MI, USA 48109
[e]Department of Astronomy and Astrophysics, University of Pennsylvania, PA, USA 16802
[f]NASA Goddard Space Flight Center, 8800 Greenbelt Rd, Greenbelt, MD 20771

**Abstract**

The Advanced Atacama Cosmology Telescope Polarimeter (AdvACT) is an upgraded instrument for the Atacama Cosmology Telescope, which uses transition-edge sensor (TES) detector arrays to measure cosmic microwave background (CMB) polarization anisotropies in multiple frequency bands. We review the integration and characterization of the final polarimeter array, which is the low frequency (LF) array, consisting of 292 TES bolometers observing in two bands centered at 27 GHz and 39 GHz. This array is sensitive to synchrotron radiation from our galaxy as well as to the CMB, and complements the AdvACT arrays operating at 90, 150 and 230 GHz to provide robust detection and removal of foreground contamination. We present detector parameters for the LF array measured in the lab, including saturation powers, critical temperatures, thermal conductivities, time constants and optical efficiencies, and their uniformity across the entire wafer.

**Keywords**: CMB, AdvACT, CE7, detector array integration, low frequency TES, saturation power, time constant

## 1. INTRODUCTION

The Advanced Atacama Cosmology Telescope Polarimeter (AdvACT) is an upgraded instrument for the 6 m Atacama Cosmology Telescope (ACT), which uses transition edge sensor (TES) detector arrays to measure cosmic microwave background (CMB) temperature and polarization anisotropies at multiple frequencies. The horn-coupled AlMn TES bolometer arrays are fabricated on 150 mm wafers, which, along with the implementation of a new type of time-division multiplexer, permit deployment of twice the total number of TESes as compared to the previous receivers on ACT[1, 2] and improves the array sensitivity. The multichroic arrays, including one high frequency (HF), two middle frequency (MF) and one low frequency (LF), cover five bands from 29 GHz to 230 GHz. The improved sensitivity and resolution and the wide observing band enable AdvACT to make measurements of intensity and small angular scale polarization anisotropies of the CMB to constrain the sum of neutrino masses, dark matter and dark energy. The measurement of the CMB polarization at large angular scales to search for primordial gravitational waves. More information on AdvACT can be found in Crowley et al. 2018[3], Gallardo et al. 2018[4] and Koopman et al. 2018[5] in this 2018 SPIE conference proceedings, as well as Koopman et al. 2016[6], Bernandis et al. 2016[7], and Rojas et al. 2016[8].

Further author information: (sent to Y.L.)
Y.L.: Email: yaqiongl@princeton.edu

Millimeter, Submillimeter, and Far-Infrared Detectors and Instrumentation for Astronomy IX,
edited by Jonas Zmuidzinas, Jian-Rong Gao, Proc. of SPIE Vol. 10708, 107080A
 · doi: 10.1117/12.2313942

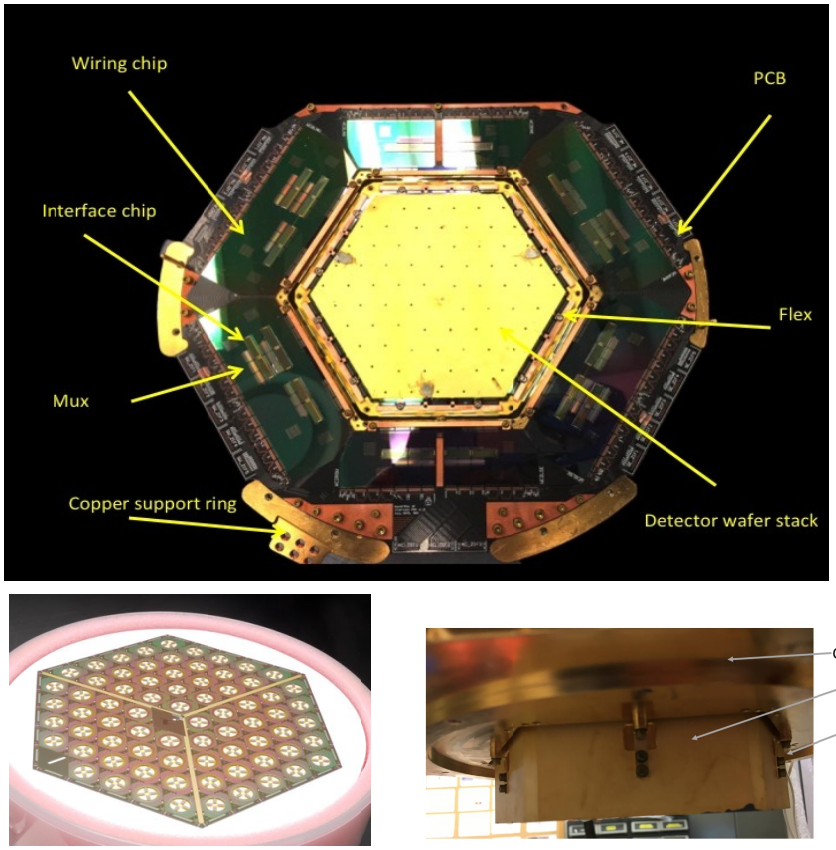


Figure 1. (Top) Components of the LF detector array, looking at the back of the detector array stack. The hexagonal detector wafer stack is surrounded by an annular printed circuit board (PCB) mounted on a copper support ring, which also heat sinks the array. Large silicon wiring chips are glued to the PCB. Interface chips, providing shunt resistors and series inductors, and multiplexing chips are die bonded on top of the wiring chips. The time division multiplexing system is described in Doriese et al. 2016[13]. Each TES is inductively coupled to a SQUID. The wiring associates each detector with a row and a column. Activating a single row of SQUIDs while summing all the current from 25 rows of SQUIDs associated with a single column allows one to read a single TES signal per column at one time. (Bottom right) The feedhorn array is mounted to the bottom of the copper support ring through six L-brackets on its sides. The sky side of the feedhorn array is pointing down in this photograph, and three L-brackets are visible. (Bottom left) The LF detector wafer. The 73 OMTs are clearly visible as four-lobed patterns on nearly transparent circular membranes. Note that the center is used for an alignment pin. The alignment slot is visible near the lower left corner of the hexagon.

One HF and two MF arrays were deployed at the 5200 m altitude site in Chile in July 2016 and April 2017, respectively, and they have been observing the CMB since their installation. The LF array has been tested extensively in the laboratory, and will be fielded in place of one of the MF arrays in Spring 2019. In this proceeding, we will review the integration and characterization of the LF array. The LF detector array couples to an array of 73 feedhorns. The array has 292 optical TESes for observing CMB radiation and its polarization in two bands centered at 27 GHz and 39 GHz and 98 dark TESes for monitoring bath temperature variation during the observation. This array is sensitive to synchrotron radiation from galactic emission as well as to the CMB, and complements the AdvACT HF and MF arrays operating at 90, 150 and 230 GHz to enable robust detection and removal of contamination by astrophysical foregrounds. First, in Section 2 we will describe new methods of assembly relative to those used for the HF and MF arrays to accommodate the use of a new feedhorn material (an aluminum silicon alloy rather than silicon[9]), and changes in the mechanical design of the detector wafer and associated parts. We next present the LF array characterization in Section 3 with parameters measured in the lab, including saturation powers at 100 mK bath temperature, superconducting critical temperatures, thermal conductivities, and time constants. Finally, in Section 4 we discuss the optical efficiencies measured with a cold load

as a blackbody radiation source, and the time constants measured in a loading environment comparable to that expected in the field. The parameters are analyzed from current-voltage (IV) curves and data with small square waves injected on top of the DC bias voltage provided to the TES (bias step data), measured under a variety of bath temperatures. We will conclude with the detector yield and the uniformity across the entire wafer.

## 2. INTEGRATION PROCESS

The four Advanced ACTPol arrays share great similarities in electrical and mechanical structure[10]. The array components are shown in Figure 1. The hexagon-shaped detector wafer stack consists of the detector wafer and additional wafers to provide waveguide quarter-wave backshorts and waveguide interfaces to the planar orthomode transducers (OMTs) on the detector wafer, as shown in Figure 1. Four AlMn TESes, for two frequencies and two polarizations, are optically coupled to each of the 73 spline-profile horns through an OMT. Six superconducting flexible cables (flex) transfer the TES signals to the interface chips, which provide 6 mΩ shunt resistors for TES voltage biasing, and to the two-stage superconducting quantum interference device (SQUID) multiplexing system[11]. The signals are finally read out by room-temperature multichannel electronics (MCE)[12] crates provided by the University of British Columbia.

The LF array differs from the other AdvACT arrays in several ways. The LF array has larger pixels and therefore far fewer optical pixels (73 rather than 503 or 429 for the HF and MF arrays, respectively), but many more dark TESes. There is one dark TES per frequency per pixel to monitor bath temperature variation, 98 of which are connected to the readout system. The LF array has fewer than half the number of mux and interface chips compared to the MF array because of the reduced number of detectors. Finally, the LF feedhorn array is directly machined out of an aluminum-silicon alloy (CE7) block[9], instead of stacking multiple layers of etched silicon wafer as in the HF and MF arrays[14, 15]. The feedhorn no longer has choke features. As shown in Figure 2, we instead realize waveguide choke features in silicon. We couple the silicon parts to the CE7 block using two alignment pins. One of the pins is seated in a radially-oriented slot to permit relative motion due to the differential thermal contraction (see Figure 1, lower right).

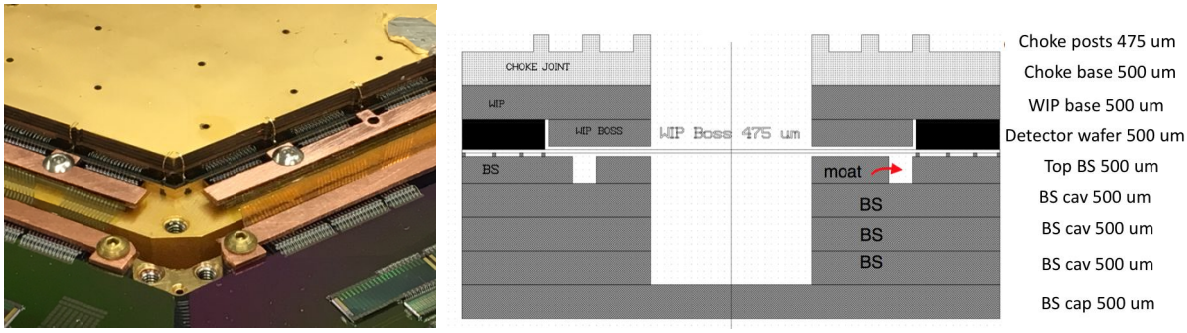


Figure 2. (Left) A picture of flex and detector wafer area. Each flex is bolted down by two copper bars with two low profile screws and two alignment pins. There are also four to five gold ribbon bonds on each edge of the wafer from the top of the backshort cap (the top gold surface in the photo) to the detector wafer to improve detector heat sinking. (Right) The cross section of the detector wafer stack. The feedhorn array is not shown, but mounts above the choke joint wafer; thus, this figure is oriented upside down with respect to the photo on the left. The thickness of each silicon wafer is shown on the right. The waveguide interference plate (WIP) extends the circular waveguide from the feedhorn input aperture down to the membrane upon which the OMT is suspended. The detector wafer is shown in black. The backshort (BS) is a metallized wafer at the bottom of a 2 mm deep cavity. The moats in the "top BS" wafer are filled with absorber to suppress surface waves between detectors.

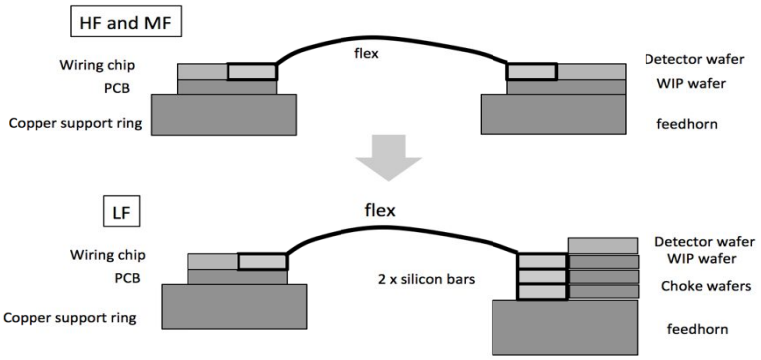


Figure 3. Sketch of the mounting of the superconducting flex used to connect the TESes on the detector wafer to the wiring chips shown in Figure 1. The flex comprises a flexible polyimide section attached to silicon stiffeners at each end. The stiffeners, the wiring chips, and the detector wafers are 0.5 mm thick. For all of the arrays, one of the flex stiffeners rests on top of the PCB (shown on the left of the sketch), leaving the bond pads on the flex at the same height as the bond pads on the wiring chip. The top panel shows that for the HF and MF arrays, the WIP wafer is wider than the detector wafer, so that the flex stiffener can rest on the WIP wafer. This allows room for the flex stiffener to mount to the WIP wafer so that the bond pads on the flex and on the detector wafer are at the same height. The bottom panel shows that for LF, the WIP wafer and the detector wafer have the same edge-to-edge extent, so the flex stiffener for the LF array must sit on top of the feedhorn array. Several 0.5 mm silicon bars are used to raise the flex until its bond pads are only 0.5 mm lower than the bond pads on the detector wafer.

The integration of the LF array is similar to that of the HF array, which is described in Li et al. 2016[16], except for one major change in the flex mounting. The flex is a stack of polyimide layers containing aluminum traces with a 5 mm wide silicon stiffener on both ends. In the HF and MF arrays, as shown in the top panel of Figure 3, the waveguide interface wafer (WIP) extends 5 mm beyond the edge of the detector wafer, and each flex is mounted with one side of its silicon stiffener glued on the WIP right next to the detector wafer and the other side glued on the PCB right next to the wiring chip. In LF, the pixels are larger. To accommodate the maximum number of pixels with a 13.4 mm pixel pitch, the detector wafer's edge-to-edge distance is 5.5 mm larger than that in HF and MF, making it challenging to fabricate a WIP wafer large enough for the previous scheme. Instead, we design the WIP size to be the same as the detector wafer and mount the flex directly to the feedhorn. The flex stiffener first gets stycasted to two 0.5 mm thick bars of silicon to make up the height difference between the 2 mm tall detector wafer stack and the 0.5 mm tall stiffener. It is then bolted on the feedhorn with low profile screws and a 0.8 mm thick copper bar, as shown in the bottom panel of Figure 4. This attachment method accommodates the difference between the coefficients of thermal expansion of CE7 and silicon.

# 3. DARK PARAMETER TESTING

## 3.1 DARK PARAMETER TESTING SETUP

The LF testing largely followed Ho et al. 2016[17] for the AdvACT HF array and Choi et al. 2017[18] for the MF arrays, except that for LF, the dark parameters and optical efficiency were tested in separate cryogenic cooldowns of the dilution refrigerator test cryostat. In the dark parameter characterization, all of the feedhorns were covered by a metal cover, which mounted to the copper support ring (see Figure 1) and therefore was heat sunk to the bath temperature. To prevent the cover from being heated by radiation from the fridge's higher temperature stages, we attached five layers of superinsulation film to its outer surface.

## 3.2 DARK PARAMETER TESTING RESULTS

To characterize the TES thermal conductivity, we assume that the power heating the TES and the temperature of the TES are related by a power law:

$$P_\gamma + P_{bias} = \kappa(T^n - T_{bath}^n), \quad (1)$$

where $P_\gamma$ is the optical power on the TES, $P_{bias}$ is the electrical power dissipated in the nonzero resistance of the TES, $T$ is the TES island temperature (taken to be $T_c$, the superconducting critical temperature), $n$ is the power law index, and $\kappa$ is related to the thermal coupling between the island and the bath, and $\kappa(T^n - T_{bath}^n)$ represents the heat transferred from the TES island to the thermal bath. The saturation power $P_{sat}$ is defined as the total power needed to drive the TES resistance to 90% of its normal resistance. In our dark testing setup, $P_\gamma$ is approximately zero; therefore Eq. 1 becomes:

$$P_{sat} = P_{bias} = \kappa(T_c^n - T_{bath}^n). \quad (2)$$

We can relate G, the thermal conductance of the thin leg connecting the TES island and the bath, to $\kappa$ and $n$:

$$G = \frac{dP}{dT}|_{T=T_c} = n\kappa T_c^{n-1}. \quad (3)$$

By fitting Eq. 2 to $P_{sat}$ values at different bath temperatures, $n$, $\kappa$, and $T_c$ can be estimated.

During data acquisition, we first drive the TES to its normal state and slowly ramp down the bias voltage to measure the TES's IV curves. In each IV curve, 2000 bias points are taken. We ramp the bath temperature from 75 mK to 160 mK in steps of 5 mK or 10 mK and take IV curves at each $T_{bath}$. Since the atmospheric emission is much smaller at 27 GHz than at 39 GHz, the targeted $P_{sat}$ values for the two frequencies are significantly different[19], and the initial bias power needed to drive the 39 GHz detectors normal is relatively large and may cause enough $T_{bath}$ variation to have a significant thermal effect on the 27 GHz detectors. Therefore, at each $T_{bath}$, we separate the TESes by their frequencies and only take IV curves at one frequency at a time to control the $T_{bath}$ variation within 2 mK.

For the fitting, we assume the uncertainties in $P_{sat}$ are the same at different $T_{bath}$. Since $n$ and $\kappa$ are both related to the geometry of the TES legs, there is strong degeneracy between $n$ and $\kappa$, while $T_c$ remains independent. To confirm the $n$ - $\kappa$ degeneracy, we do 3-parameter fitting and then fix $n$ at the median of the result and do the fitting again for $\kappa$ and $T_c$ only. The result shows that $T_c$ and the calculated $G$ from the 3-parameter fitting are within 3% of the results from the 2-parameter fitting. Figure 4 and Figure 5 show the distributions of $P_{sat}$ at 100 mK bath temperature, $G$ and $T_c$ from 3-parameter fitting. The median values and standard deviations of those parameters and the index $n$ are given in Table 1, along with the array yield.

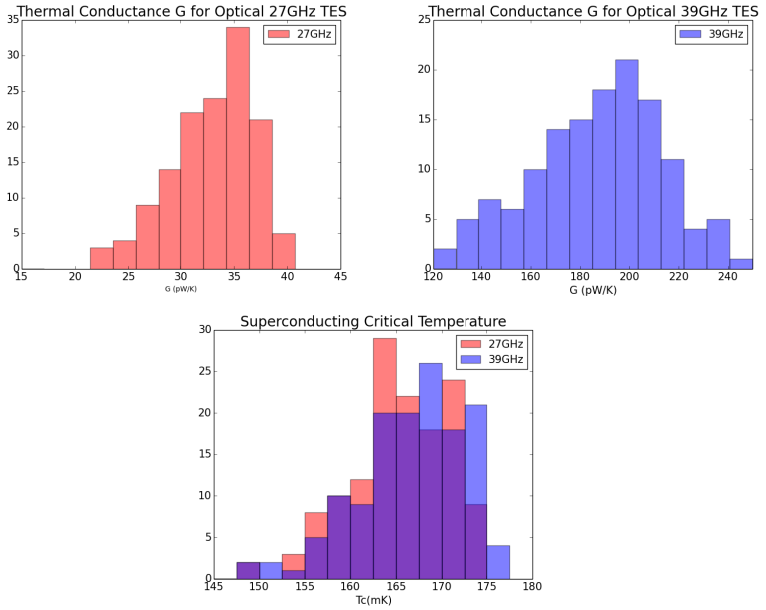


Figure 4. Histograms of $G$ and $T_c$ for the LF array from dark tests. The top row shows $G$ for the "optical" bolometers (those coupled to feedhorns) for 27 GHz (left) and 39 GHz (right). The bottom figure shows $T_c$ for both the 27 GHz and 39 GHz bolometers, illustrating great uniformity across the array, with standard deviation less than 4% of the median.

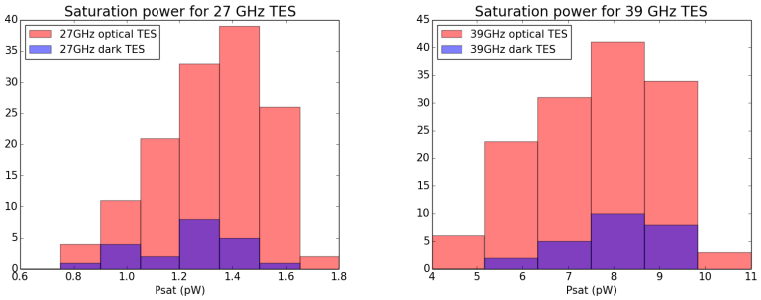


Figure 5. Histograms of $P_{sat}$ at bath temperature 100 mK, with results from "dark" bolometers (those not coupled to feedhorns) shown along with results from optical bolometers. The median $P_{sat}$ values are 1.2 pW for the 27 GHz bolometers and 7.1 pW for the 39 GHz bolometers, which are close to the targeted values of 1.5 pW and 7.8 pW.

| Parameters | $P_{sat}$ (pW) | $T_c$ (mK) | $G$ (pW/K) | $n$ | Yield (%) |
|---|---|---|---|---|---|
| 27 GHz | 1.3 ± 0.2 | 165.5 ± 5.3 | 33.3 ± 3.8 | 3.5 ± 0.1 | 93.8 |
| 39 GHz | 7.8 ± 1.4 | 167.5 ± 5.9 | 188.7 ± 27.4 | 3.3 ± 0.2 | 92.5 |

Table 1. The median and standard deviation of the dark parameters from 3-parameter fitting of the IV curves taken at a range of bath temperatures. The yield, given in the last column, is defined as the number of optical bolometers with analyzable IV curves relative to the 292 fabricated on the array.

# 4. OPTICAL TESTING

## 4.1 OPTICAL TESTING SETUP

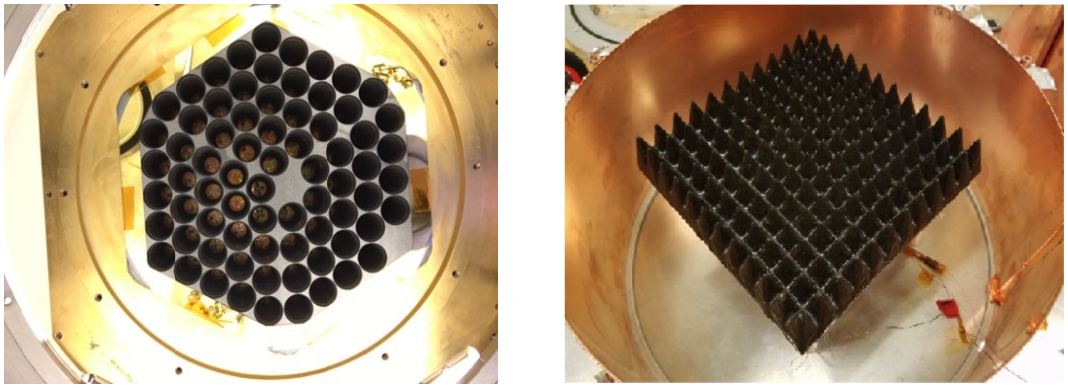

Figure 6. (Left) The sky side of the feedhorn array. The perimeter of the array is covered with a gold-plated silicon frame to improve its reflectivity in the infrared. (Right) The cold load. Three low pass filters are mounted between the cold load and the feedhorn array. Photo courtesy of Choi et. al. 2017[18].

In the optical testing setup, we illuminate the entire array with a cold load black body radiation source as shown in Figure 6. The cold load is mounted 9.5 cm below the bottom surface (the sky side) of the feedhorn array. The cold load is a 15 cm by 15 cm square array of aluminum pyramids coated with Eccosorb-101. Three low pass filters, with frequency cutoffs at 5.85 $cm^{-1}$, 8.5 $cm^{-1}$ and 12 $cm^{-1}$, are mounted between the cold load and feedhorn array, and are heat sunk at the 100 mK, 1 K and 4 K stages, respectively. As shown in Figure 5, we also put a 250 μm thick gold-plated silicon frame on the feedhorn array to minimize the heat absorbed by the superconducting CE7 feedhorn array, which is only gold-plated on its sides.

## 4.2 OPTICAL TESTING RESULTS

We use data taken with the detectors viewing the cold load to estimate the detector efficiencies and to estimate their time constants under loading conditions comparable to the loading expected in the field. We begin by describing the procedure for estimating detector efficiencies, which largely follows Crowley et. al. 2016[20] (for the HF array) and

Choi et. al. 2017[18] (for the MF arrays). For each cold load temperature $T_{CL}$, the optical power $P_\gamma^{CL}$ impinging on a bolometer in the LF array can be estimated by

$$P_\gamma^{CL}(T_{CL}) = \frac{1}{2}\int \varepsilon(\nu) f(\nu) A_e(\nu) P(\theta,\varphi,\upsilon) B(\nu, T_{CL}) d\Omega d\nu, \quad (4)$$

where $\nu$ is the frequency, $\epsilon(\nu)$is the cold load emissivity, $f(\nu)$ is the product of the transmissions of the three low pass filters, and $A_e(\nu)$ is the effective area of the feedhorn and is equal to $\lambda^2/\Omega$, where $\Omega$ stands for the total solid angle of the feedhorn beam. The simulated normalized beam pattern of the feedhorn is $P(\theta,\varphi,\upsilon)$, and $B(\nu, T_{CL})$ is the Planck function. The factor of ½ accounts for the fact that each detector is sensitive to only one linear polarization. By integrating over the solid angle, Eq.4 can then be written as:

$$P_\gamma^{CL}(T_{CL}) = \frac{1}{2}\int \varepsilon(\nu) f(\nu) \frac{c^2}{\nu^2}\frac{\Omega_{CL}(\nu)}{\Omega_{total}(\nu)} B(\nu, T_{CL}) d\nu, \quad (5)$$

where $\Omega_{CL}(\nu)$ and $\Omega_{total}(\nu)$ are the integrals of the feedhorn beam over the solid angle subtended by the cold load, and over all space, respectively.

We fix the bath temperature at 75 mK, ramp the cold load temperature from 11.5 K to 16 K in 0.5 K steps and measure each detector's $P_{sat}$ at each $T_{CL}$. Although the array bath temperature is fixed, the local bath temperature for each TES might vary. To account for real bath temperature variations caused by changing $T_{CL}$, we use the dark TESes. We assume the array is radially symmetric, and estimate the real bath temperature from Eq. 6,

$$T_{bath} = < T_{bath}^{dark} > = < [(T_c^{dark})^{n^{dark}} - P_{sat}^{dark}]^{\frac{1}{n^{dark}}} >, \quad (6)$$

where $< T_{bath}^{dark} >$ is the average $T_{bath}$ of all the dark TESes in an annulus around the array center, with its radial extent defined to be ± 1cm around the radius of the target optical bolometer. $n^{dark}$, $\kappa^{dark}$ and $T_c^{dark}$ are dark parameters for the dark TESes, and each $T_{bath}^{dark}$ is calculated from the inverse function of Eq. 1. We then calculate the saturation power of the optical TES without the optical load to be:

$$P_{sat}^{cali} = \kappa^{opt}(T_c^{opt})^{n^{opt}} - \kappa^{opt} < T_{bath}^{dark} >^{n^{opt}}, \quad (6)$$

where $n^{opt}$, $\kappa^{opt}$ and $T_c^{opt}$ are dark parameters for the optical-coupled TES. We estimate the optical power absorbed in each optically-coupled bolometer, $P_\gamma^{abs}$, from $P_\gamma^{abs} = P_{sat}^{cali} - P_{sat}$. We then assume $P_\gamma^{abs}$ is proportional to $P_\gamma^{CL}$ and fit to a linear function,

$$P_\gamma^{abs} = \eta\, P_\gamma^{CL} + P_{DC}, \quad (7)$$

to find the optical efficiency $\eta$. We treat $P_{DC}$ as a constant offset, arising from the unspecified saturation powers of the bolometers in the dark at constant bath temperature, and possibly from thermal radiation from other parts of the cryostat.

We present results for the optical efficiency estimates for the 39 GHz bolometers in the left panel of Figure 7. The errors for each measurement are estimated as ~20%, and are dominated by systematic effects from estimation of dark detector corrections for thermal bath variations, which are imperfectly estimated with the small number of TESes in each radial bin[20]. We do not present optical efficiencies for 27 GHz bolometers because systematic errors are comparatively larger for those low power devices since the cold load only subtends about 1/3 of the total solid angle of the 27 GHz beam. We are currently investigating the possibility that the possible bimodality of the distribution for 39 GHz bolometers may be related to their polarization.

Finally, we use data taken with the cold load at 11 K and the bath temperature at 100 mK to estimate the time constants of the detectors. The time constant $\tau$ is measured as the time a TES takes to decay by $1/e$ from the peak value of a small square wave in its voltage bias. The right panel of Figure 6 shows histograms of $f_{3dB} \equiv 1/(2\pi\tau)$ for the optically-coupled bolometers, with the DC values of the 12 voltage bias lines set to center the distribution of TES resistances at 40% of their normal resistances.

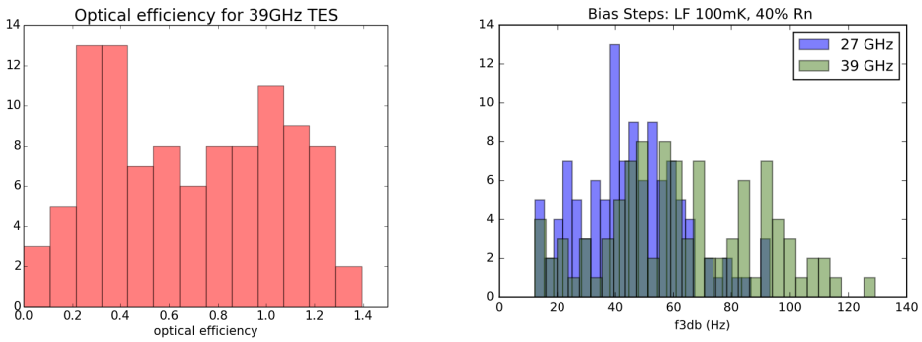


Figure 7. (Left) Histogram of the TES optical efficiencies. (Right) Time constant result taken at 40% Rn when the detector array was facing 11K cold load, which is approximately the signal expected from the sky with atmosphere precipitable water vapor (PWV) ~1 mm. The median $f_{3db}$ (44.4 Hz and 60.9 Hz for 27 GHz and 39 GHz detectors, respectively) is good but the distribution includes slower detectors than the targeted value, which is 25 Hz.

## 5. SUMMARY

The final detector array for the Advanced ACT Polarimeter has been assembled and tested in the laboratory. The TES yield for the 292 optically-coupled bolometers is over 90% for each of the two frequency bands, which are centered at 27 and 39 GHz. The device parameters, $P_{sat}$, $G$ , $T_c$ have been measured in the absence of optical signals and found to be close to the targeted values, and exhibit good uniformity. The bolometers' optical efficiencies and time constants have also been estimated in separate tests with a ~10 K cold load. Though these parameters exhibit a wider spread than anticipated, the average performance is good, and we intend to deploy the array on the Atacama Cosmology Telescope at the Parque Astronómico Atacama in northern Chile in the Spring 2019.

## ACKNOWLEDGEMENTS

This work was supported by the U.S. National Science Foundation through MSIP award AST-1440226. The development of multichroic detectors was supported by NASA grant NNX14AB58G. The work of KTC, NFC, BJK, and JTW was supported by NASA Space Technology Research Fellowship awards.

## REFERENCES

[1] Swetz, D. S., Ade, P. A. R., Amiri, M., Appel, J. W., Battistelli, E. S., Burger, B., Chervenak, J., Devlin, M. J., Dicker, S. R., et al., "Overview of the Atacama Cosmology Telescope: Receiver, Instrumentation and Telescope Systems", ApJS, 194, 41 (2011).

[2] Thornton, R. J., Ade, P. A. R., Aiola, S., Angile, F. E., Amiri, M., Beall, J. A., Becker, D. T., Cho, H., et al., "The Atacama Cosmology Telescope: The Polarization-sensitive ACTPol instrument", ApJS, 227, (2016).

[3] Crowley, K., et. al., "Electrothermal characterization of AlMn transition edge sensor bolometers for Advanced ACTPol Telescope," Proc. SPIE, (2018).

[4] Gallardo, P., et. al., "Far sidelobes from baffles and telescope support structures in the Atacama Cosmology Telescope," Proc. SPIE, (2018).

[5] Koopman, B., et. al., "Advanced ACTPol: telescope systems and project status," Proc. SPIE, (2018).

[6] Koopman, B., Austermann, J., Cho, H.-M., Coughlin, K. P., Duff, S. M., Gallardo, P. A., Hasselfield, M., Henderson, S. W., Ho, S.-P. P., et al., "Optical modeling and polarization calibration for CMB measurements with ACTPol and Advanced ACTPol," Millimeter, Submillimeter, and Far-Infrared Detectors and Instrumentation for Astronomy VIII (2016).

[7] De Bernardis, F., Stevens, J. R., Hasselfield, M., Alonso, D., Bond, J. R., Calabrese, E., Choi, S. K., Crowley, K. T., Dunkley, J., et al., "Survey strategy optimization for the Atacama Cosmology Telescope," Millimeter, Submillimeter, and Far-Infrared Detectors and Instrumentation for Astronomy VIII (2016).

[8] Rojas, P. A. F., Dünner, R., Maurin, L., Choi, S. K., Devlin, M. J., Gallardo, P. A., Ho, S.-P. P., Koopman, B. J., Louis, T., et al., "Far sidelobe effects from panel gaps of the Atacama Cosmology Telescope," Millimeter, Submillimeter, and Far-Infrared Detectors and Instrumentation for Astronomy VIII (2016).
[9] Simon, S. M., Beall, J. A., Cothard, N. F., Duff, S. M., Gallardo, P. A., Ho, S. P., Hubmayr, J., Koopman, B. J., Mcmahon, J. J., et al., "The Advanced ACTPol 27/39 GHz Array," Journal of Low Temperature Physics (2018).
[10] Ward, J. T., Austermann, J., Beall, J. A., Choi, S. K., Crowley, K. T., Devlin, M. J., Duff, S. M., Gallardo, P. A., Henderson, S. W., et al., "Mechanical designs and development of TES bolometer detector arrays for the Advanced ACTPol experiment," Millimeter, Submillimeter, and Far-Infrared Detectors and Instrumentation for Astronomy VIII (2016).
[11] Henderson, S. W., Stevens, J. R., Amiri, M., Austermann, J., Beall, J. A., Chaudhuri, S., Cho, H.-M., Choi, S. K., Cothard, N. F., et al., "Readout of two-kilopixel transition-edge sensor arrays for Advanced ACTPol," Millimeter, Submillimeter, and Far-Infrared Detectors and Instrumentation for Astronomy VIII (2016).
[12] Battistelli, E. S., Amiri, M., Burger, B., Halpern, M., Knotek, S., Ellis, M., Gao, X., Kelly, D., Macintosh, M., et al., "Functional Description of Read-out Electronics for Time-Domain Multiplexed Bolometers for Millimeter and Sub-millimeter Astronomy," Journal of Low Temperature Physics 151(3-4), 908–914 (2008).
[13] Doriese, W. B., Morgan, K. M., Bennett, D. A., Denison, E. V., Fitzgerald, C. P., Fowler, J. W., Gard, J. D., Hays-Wehle, J. P., Hilton, G. C., et al., "Developments in Time-Division Multiplexing of X-ray Transition-Edge Sensors," Journal of Low Temperature Physics 184(1-2), 389–395 (2015).
[14] Yoon, K. W., Appel, J. W., Austermann, J. E., Beall, J. A., Becker, D., Benson, B. A., Bleem, L. E., Britton, J., Chang, C. L., et al., "Feedhorn-Coupled TES Polarimeters for Next-Generation CMB Instruments," AIP 1185, 515 (2009).
[15] Simon, S. M., Austermann, J., Beall, J. A., Choi, S. K., Coughlin, K. P., Duff, S. M., Gallardo, P. A., Henderson, S. W., Hills, F. B., et al., "The design and characterization of wideband spline-profiled feedhorns for Advanced ACTPol," Millimeter, Submillimeter, and Far-Infrared Detectors and Instrumentation for Astronomy VIII, (2016).
[16] Li, Y., Choi, S., Ho, S.-P., Crowley, K. T., Salatino, M., Simon, S. M., Staggs, S. T., Nati, F., Ward, J., et al., "Assembly and integration process of the first high density detector array for the Atacama Cosmology Telescope," Millimeter, Submillimeter, and Far-Infrared Detectors and Instrumentation for Astronomy VIII (2016).
[17] Ho, S.-P. P., Austermann, J., Beall, J. A., Choi, S. K., Cothard, N. F., Crowley, K. T., Datta, R., Devlin, M. J., Duff, S. M., et al., "Highly uniform 150 mm diameter multichroic polarimeter array deployed for CMB detection," Millimeter, Submillimeter, and Far-Infrared Detectors and Instrumentation for Astronomy VIII (2016).
[18] Choi, S. K., Austermann, J., Beall, J. A., Crowley, K. T., Datta, R., Duff, S. M., Gallardo, P. A., Ho, S. P., Hubmayr, J., et al., "Characterization of the Mid-Frequency Arrays for Advanced ACTPol," Journal of Low Temperature Physics (2018).
[19] Koopman, B. J., Cothard, N. F., Choi, S. K., Crowley, K. T., Duff, S. M., Henderson, S. W., Ho, S. P., Hubmayr, J., Gallardo, P. A., et al., "Advanced ACTPol Low-Frequency Array: Readout and Characterization of Prototype 27 and 39 GHz Transition Edge Sensors," Journal of Low Temperature Physics (2018).
[20] Crowley, K. T., Choi, S. K., Kuan, J., Austermann, J. A., Beall, J. A., Datta, R., Duff, S. M., Gallardo, P. A., Hasselfield, M., et al., "Characterization of AlMn TES impedance, noise, and optical efficiency in the first 150 mm multichroic array for Advanced ACTPol," Millimeter, Submillimeter, and Far-Infrared Detectors and Instrumentation for Astronomy VIII (2016).